Supplementary Information for "Check-probe spectroscopy of lifetime-limited emitters in bulk-grown silicon carbide"

Supplementary Note 1. Spectral dynamics model derivation

The Lorentzian spectral propagator is given by [1]:

$$P_f(t) = \pi^{-1} \frac{\frac{1}{2}\gamma(t)}{f^2 + \left(\frac{1}{2}\gamma(t)\right)^2}, \tag{S1}$$

where f is the detuning from resonance. The FWMH $\gamma(t)$ is linear in time [1]:

$$\gamma(t) = \gamma_\mathrm{d}\, t. \tag{S2}$$

The mean detected counts a function of detuning f between the laser and the emitter's resonance frequency is given by a Lorentzian:

$$\lambda_\mathrm{L}(f) = C_0 \frac{\left(\frac{\Gamma}{2}\right)^2}{f^2 + \left(\frac{\Gamma}{2}\right)^2}, \tag{S3}$$

with C_0 the observed counts on resonance and Γ the emitters homogeneous line width (FWHM). This Lorentzian is normalised such that $\lambda(0) = C_0$. We can add the effect of ionisation by describing the ionisation probability as:

$$P_\mathrm{i}(t) = 1 - e^{-\gamma_\mathrm{i} t}, \tag{S4}$$

Here, γ_i is assumed to be independent of emitter detuning. However, if ionisation is caused by a two-photon process, we would expect the ionisation rate to scale with the square of the excitation rate:

$$\gamma_\mathrm{i}(f) = \gamma_\mathrm{i}^0 \left(\frac{(\frac{1}{2}\Gamma)^2}{f^2 + (\frac{1}{2}\Gamma)^2}\right)^2, \tag{S5}$$

where γ_i^0 is the ionisation rate on resonance. Then,

$$\gamma_\mathrm{i} = \int_{-\infty}^{\infty} P_f\, \gamma_\mathrm{i}(f) df = \frac{\gamma_i^0}{2} \frac{\Gamma\gamma(t) + 2\Gamma^2}{(\gamma(t) + \Gamma)^2} \tag{S6}$$

The mean counts can then be calculated as:

$$\lambda(f,t) = (1 - P_\mathrm{i}(t))\ \lambda_\mathrm{L}(f), \tag{S7}$$

Next, we integrate over the spectral density:

$$C(t) = \int_{-\infty}^{\infty} P_f(t)\, \lambda(f,t)\, df, \tag{S8}$$

which can be solved to yield:

$$C(t) = C_0 \frac{1}{1 + \gamma_\mathrm{d}\, t/\Gamma} e^{-\gamma_\mathrm{i} t}. \tag{S9}$$

where we can either decide to model γ_i as a constant, or by equation (S6). Additionally, if we neglect the recapture or de-ionisation rate, then for values of $t < 0$, effectively $\gamma_i = 0$.

Supplementary Note 2. Spectral dynamics model performance and dependence on set counts threshold

The model presented in the main text describes spectral diffusion caused by a macroscopic bath of fluctuating dipoles (described by the spectral propagator in Eq. S1). We can compare the performance of this model compared to other versions of the model, which restric certain parameters, for example one that assumes that no spectral diffusion (or ionisation) occurs. Supplementary Table I presents the description of the models we fitted to the data.

Sweeping the counts threshold value T, we observe that all models saturate to a range of values for higher T, consistent with the intuition that stringent thresholds initialise the emitter more precisely on resonance with the lasers. At very high tresholds ($T \gtrapprox 35$), only very little data is available, and rates obtained with all models start to fluctuate heavily (due to the noisy data). Hence, we emperically determine a convergence region: $20 \leq T \leq 27$ (grey solid lines in Supplementary Fig. 1 and $12 \leq T \leq 21$ in Supplementary Fig. 2), over which we average to obtain the rates presented in the main text.

Comparing various goodness of fit metrics (reduced χ-squared, AIC, BIC), we learn that the 'No recap' model describes the data best (Supplementary Fig. 1j-l), indicating that recapture is virtually not present under NIR-laser illumination.

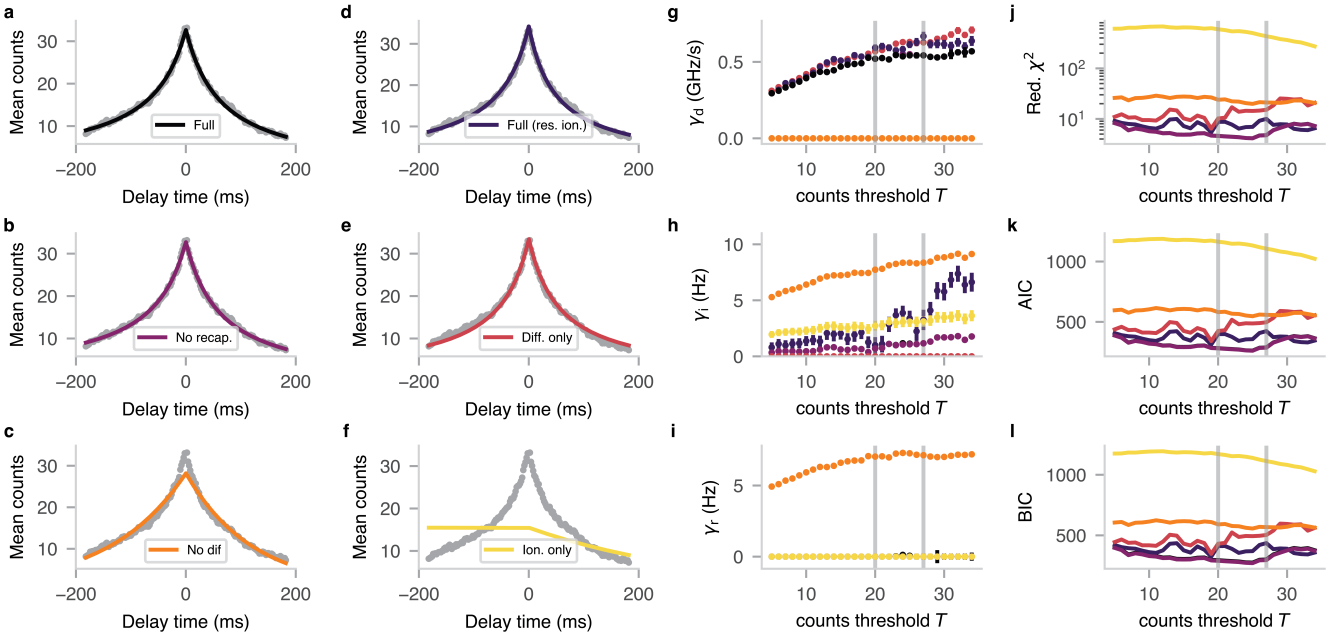

Supplementary Figure 1. **Comparison of models for perturbation by the NIR lasers. a-f)** Data from Fig. 3d, overlayed with the various models, which are described in Supplementary Table I. **g-i)** Estimated rates $\gamma_\mathrm{d}, \gamma_\mathrm{i}^0, \gamma_\mathrm{r}$ as a function of counts threshold T for the different models. We observe a saturating behaviour for high T, as the defect is initialised in a more specific frequency range. For very high treshold values, the lack of data creates large fluctuations in the obtained rates. To determine the rate values in Supplementary Table I, we take an average over the values indicated by the grey solid lines and take the standard deviation as uncertainty. **j-l)** Various goodness of fit models (reduced χ-squared, AIC, BIC) indicate that the model presented in the main text (Std.) captures the data best. Here, we also observe a saturation behaviour, where the sudden drop for very high T is attributed to overfitting due to lack of data. Colors in (g-l) match the models described in (a-f). The 'Full' data overlaps with the 'Full (res.ion.)' curve. Errorbars are based on photon shot noise (grey data), or represent fit uncertainties (panels g-i).

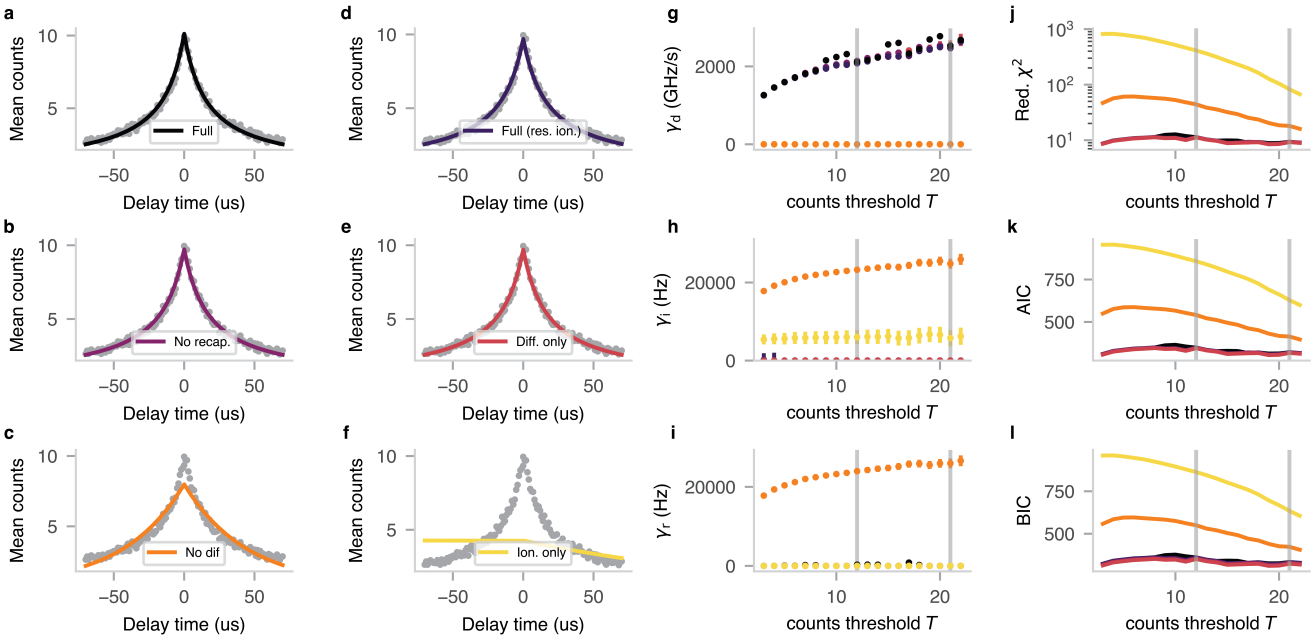

Supplementary Figure 2. **Comparison of models for perturbation by the repump laser. a-i)** Same as Supplementary Fig.1, but for the data presented in Fig. 3e.

Supplementary Table I. Models used for fitting in Supplementary Figs. 1 and 2

Model name	Description
Full	$C(t)/C_0 = \begin{cases} (1+\gamma_d\, t/\Gamma)^{-1}\, e^{-\gamma_i t}, & \text{if } t>0. \\ (1-\gamma_d\, t/\Gamma)^{-1}\, e^{\gamma_r t}, & \text{otherwise.} \end{cases}$
Full (res. ion.)	$C(t)/C_0 = \begin{cases} (1+\gamma_d\, t/\Gamma)^{-1}\, e^{-\frac{\gamma_i^0}{2}\frac{\Gamma\gamma(t)+2\Gamma^2}{(\gamma(t)+\Gamma)^2}t}, & \text{if } t>0. \\ (1-\gamma_d\, t/\Gamma)^{-1}\, e^{\gamma_r t}, & \text{otherwise.} \end{cases}$
No recap.	$C(t)/C_0 = \begin{cases} (1+\gamma_d\, t/\Gamma)^{-1}\, e^{-\gamma_i t}, & \text{if } t>0. \\ (1-\gamma_d\, t/\Gamma)^{-1}, & \text{otherwise.} \end{cases}$
Diff. only	$C(t)/C_0 = \begin{cases} (1+\gamma_d\, t/\Gamma)^{-1}, & \text{if } t>0. \\ (1-\gamma_d\, t/\Gamma)^{-1}, & \text{otherwise.} \end{cases}$
No diff.	$C(t)/C_0 = \begin{cases} e^{-\gamma_i t}, & \text{if } t>0. \\ e^{\gamma_r t}, & \text{otherwise.} \end{cases}$
Ion. only	$C(t)/C_0 = \begin{cases} e^{-\gamma_i t}, & \text{if } t>0. \\ 1, & \text{otherwise.} \end{cases}$

Supplementary Note 3. Diffusion power dependence

Here we plot the diffusion rates extracted by the method in figure 3 for different resonant and NIR laser powers. The data in figure 3 was averaged over the powers corresponding to the last two data points in figure 3a and b for the repump and NIR laser respectively.

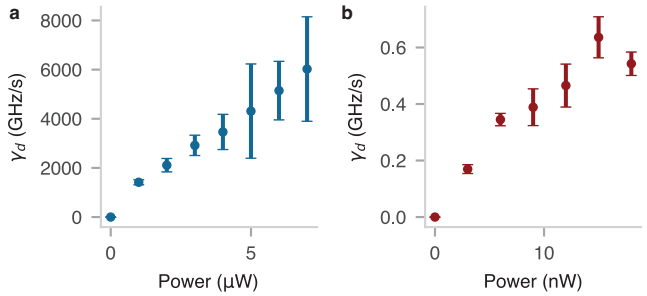

Supplementary Figure 3. **Diffusion rates as function of laser power. a)** Diffusion rate γ_d as a function of applied repump laser power (785 nm, as in Fig. 3c). Data from 8-10 μW are omitted as the CR-check was not passed, due to drifting of the objective (leading to a diminished collection efficiency). **b)** Diffusion rate γ_d as a function of applied resonant laser power (916 nm, single laser). Data points for both panels are an average over fits with thresholds $T = \{10, 14, 18\}$, and error bars denote the standard deviation of the extracted rates. Laser powers are measured at the entrance of the objective. The rates presented in Fig. 3d are an average of the two final (saturation) data points for both panels (with their standard deviation as error bar).

In another sample (same wafer and fabrication method, but with an irradiation dose of $2 \times 10^{12}\,\mathrm{cm}^{-2}$), we investigated a V2 center with significantly lower (saturation) spectral diffusion rates under NIR laser illumination ($\sim$ 6 times smaller compared to the emitter from the main text, see Supplementary Fig. 3). The extracted diffusion and ionisation rates for different NIR laser powers can be found in 4b-d. We observe a saturation-type behaviour for spectral diffusion (up to 70 nW) and an (approximately quadratic) increase in (on-resonance) ionisation rate for higher powers.

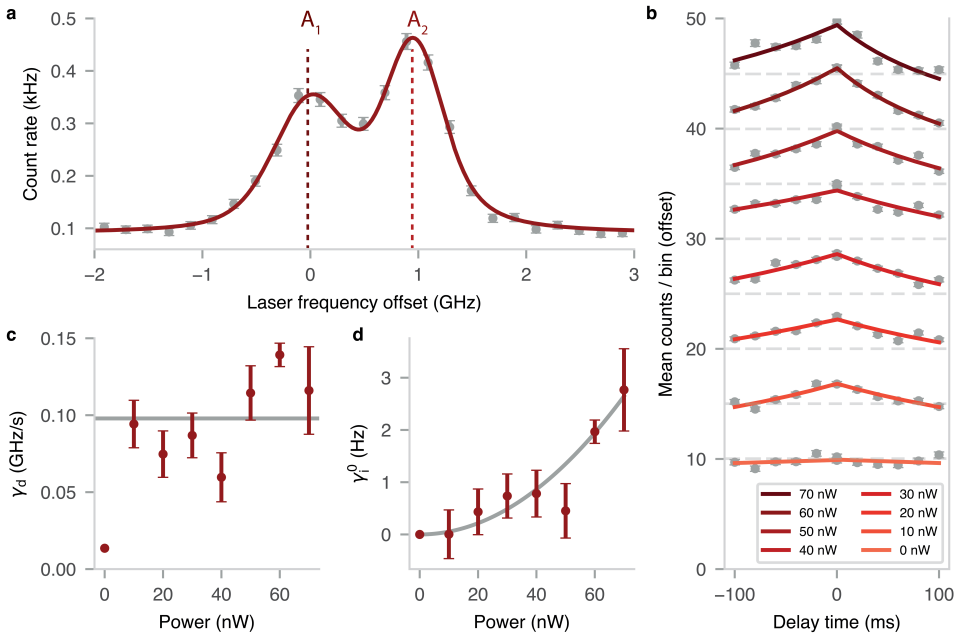

Supplementary Figure 4. **Diffusion rates of a** V2 **center in a different nanopillar a)** Diffusion-averaged PLE of the V2 center in a different nanopillar (in a different sample) compared to Fig. 1f, yielding FWHMs of ~ 802 MHz and ~ 680 MHz for the A_1 and A_2 transitions, respectively. **b)** Diffusion check-probe spectroscopy as in Fig. 3d in the main text, for different NIR-laser powers (916 nm). We explicitly set $\gamma_r = 0$ (as suggested by Supplementary Fig. 1) to ensure convergence of the fit. The grey dotted lines indicate the threshold $T = 10$ used for the 'probe' block. Data are offset by 3 for visual clarity. **c)** Diffusion rates extracted from (b). with a mean diffusion rate of $0.098\,\mathrm{GHz/s}$ **d)** (On resonance) ionisation rates extracted from (b). Solid grey line is a guide to the eye: $y = A\,x^2$, with $A = 5.4 \times 10^{-4}\,\mathrm{Hz\,nW^{-2}}$ and x the NIR laser power.

Supplementary Note 4. Bayesian analysis of the *check-probe* spectroscopy signal

The spectrum obtained from the *check-probe* spectroscopy measurements in Figs. 4 and 5 contains residual inhomogeneous broadening, due to non-perfect initialisation on-resonance with the f_1 laser frequency during the 'check' block. To account for such residual broadening, we need to considere the spectral probability density of the emitter immediately after the 'check' block, given that the minimum counts threshold T was passed. Evidently, such a spectral probability density will strongly depend on T, with higher threshold values resulting in sharper distributions around f_1. To quantify this intuition, we apply Bayes' theorem to compute the spectral probability density after detecting $m \geq T$ photons:

$$P(f \,|\, m \geq T) = \frac{P(m \geq T \,|\, f)\, P(f)}{P(m)} = \frac{1}{N_T} P(m \geq T \,|\, f)\,, \tag{S10}$$

with f the emitter frequency and N_T some (numerically determined) normalisation constant. In the second step, we have assumed minimal knowledge on the spectral distribution before the 'check' block, by taking the (improper) prior $P(f)$ to be (locally) flat. This assumption is justified if the diffusion-averaged inhomogeneous linewidth (Fig. 1f) is much larger than the homogenous linewidth (Fig. 4b). Otherwise, a different prior function may be used (e.g. the Gaussian used for fitting the data in Fig. 1f).

Assuming Poissonian photon statistics, Eq. S10 can be solved to yield:

$$P(f \,|\, m \geq T) = \frac{1}{N_T} \sum_{T}^{\infty} \frac{\lambda(f-f_1)^m\, e^{-\lambda(f-f_1)}}{m!} = \frac{1}{N_T} \left(1 - \Gamma_{\mathrm{i}}\left[T, \lambda(f-f_1)\right]\right)\,, \tag{S11}$$

with $\lambda(f)$ the expected mean number of counts during a single 'check' block when the emitter is at frequency f and the laser at frequency f_1, and $\Gamma_{\mathrm{i}}[a,z] = \frac{1}{\Gamma_{\mathrm{c}}[a]} \int_z^\infty t^{a-1} e^{-t} dt$, the incomplete Gamma function, with $\Gamma_{\mathrm{c}}[a]$ the Euler Gamma function.

Here, $\lambda(f)$ encodes (our model of) the 'pure' spectral response of the emitter, independent of residual inhomogeneous broadening, and solely governed by the underlying physical parameters whose value we aim to extract. For a simple Lorentzian lineshape, $\lambda(f)$ is given by:

$$\lambda_{\mathrm{L}}(f) = C_0 \frac{\left(\frac{\Gamma}{2}\right)^2}{f^2 + \left(\frac{\Gamma}{2}\right)^2} \tag{S12}$$

with Γ the homogeneous linewidth (FWHM) and C_0 the mean number of detected counts on resonance. Conversely, the Landau-Zener-Stückelberg spectrum can be described by (see also Eq. 6):

$$\lambda_{\mathrm{LZS}}(f) = C_0 \sum_k \frac{\Omega_k^2}{\frac{1}{T_1 T_2} + \frac{T_2}{T_1}\left(k\,\omega - f\right)^2 + \Omega_k^2}\,, \tag{S13}$$

The spectral probability densities can then be computed by inserting λ_{L} or λ_{LZS} into Eq. S11, the results of which are shown in Supplementary Fig. 5a and e, respectively.

Finally, to obtain an expression for the spectroscopy signal (i.e. the mean number of detected photons C during the probe block), we take the convolution of the spectral probability density (i.e. the residual inhomogeneous broadening) and the pure spectral response $\lambda(f)$ (assuming equal duration of the 'check' and 'probe' blocks):

$$C(f) = P(f \,|\, m \geq T) \,*\, \lambda(f)\,, \tag{S14}$$

Importantly, both terms in the convolution involve $\lambda(f)$ (through Eq. S11), and the first is strongly dependent on the chosen threshold value (see Supplementary Fig. 5a and e), allowing for the extraction of the pure spectral response by sweeping T (in post-processing). Moreover, as expected, the degree of residual inhomogeneous broadening diminishes for higher threshold values (see Fig. 5c and d).

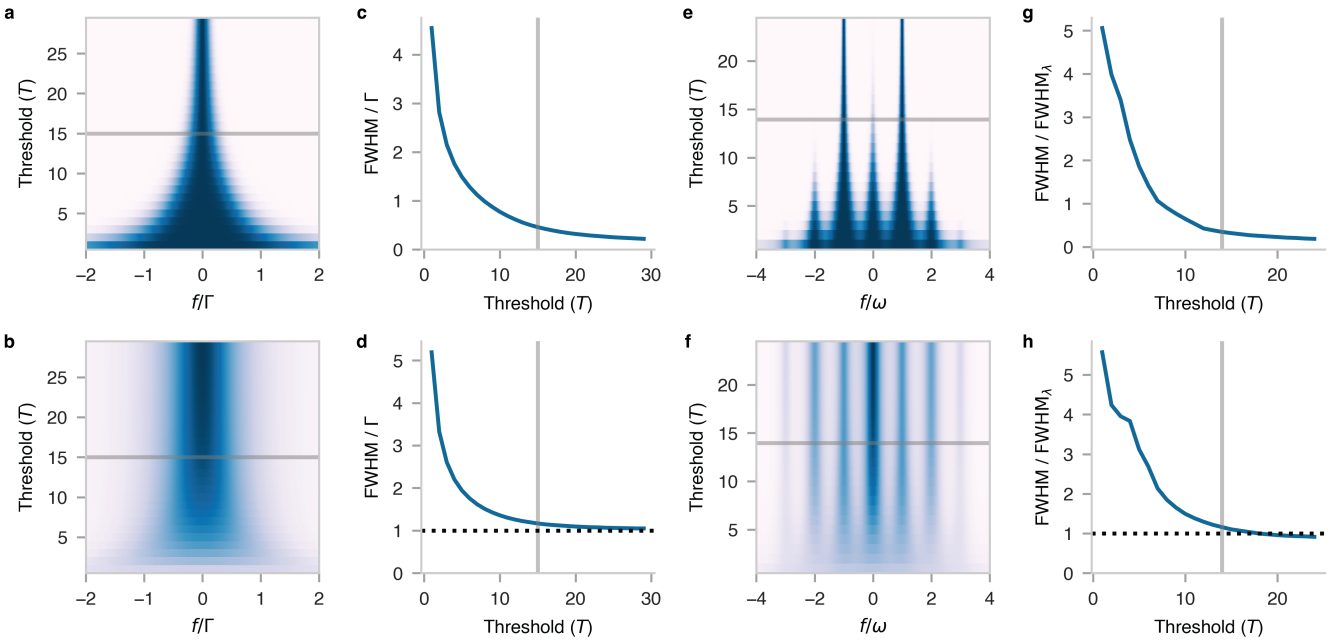

Supplementary Figure 5. **Bayesian spectrum analysis. a)** Spectral probability density $P(f \,|\, m \geq T)$ as a function of threshold for $\lambda(f) = \lambda_{\mathrm{L}}(f)$ (Lorentzian, Eq. S12). Probabilities at each threshold value are normalised to their maximum value for visual clarity. Solid grey line denotes the maximum of $\lambda(f)$ for all panels. **b)** Check-probe spectroscopy signal, obtained by evaluating Eq. S14 for the spectral density calculated in (a). **c)** Full width at half maximum (FWHM) of the spectral density in (a). In the high-threshold regime ($T \gg \max[\lambda(f)]$, the linewidth becomes negligible compared to the linewidth of $\lambda(f)$ itself. **d)** Linewidth of the spectroscopy signal, which converges to that of the pure spectral response $\lambda(f)$ for high thresholds (black dotted line). **e)** Same as in (a), but for $\lambda(f) = \lambda_{\mathrm{LZS}}(f)$, which has two global maxima (Eq. S13). LZS parameters are chosen to be equal to those extracted from the 6.5 V measurement in the main text (see Fig. 5 and Supplementary Fig. 6). **f)** Same as in (b), but for the spectral density calculated in (e). **g)** FWHM of (e), computed by integrating the frequency ranges for which $P(f \,|\, m \geq T) > \frac{1}{2} \max[P(f \,|\, m \geq T)]$ (and normalised to the range for which: $\lambda_{\mathrm{LZS}}(f) > \frac{1}{2} \max[\lambda_{\mathrm{LZS}}(f)]$). **h)** Same as in (d), but for the signal shown in (f). Note that for the LZS spectrum, which contains multiple global maxima, the FWHM does not neccesarily converge to the FWHM of $\lambda(f)$.

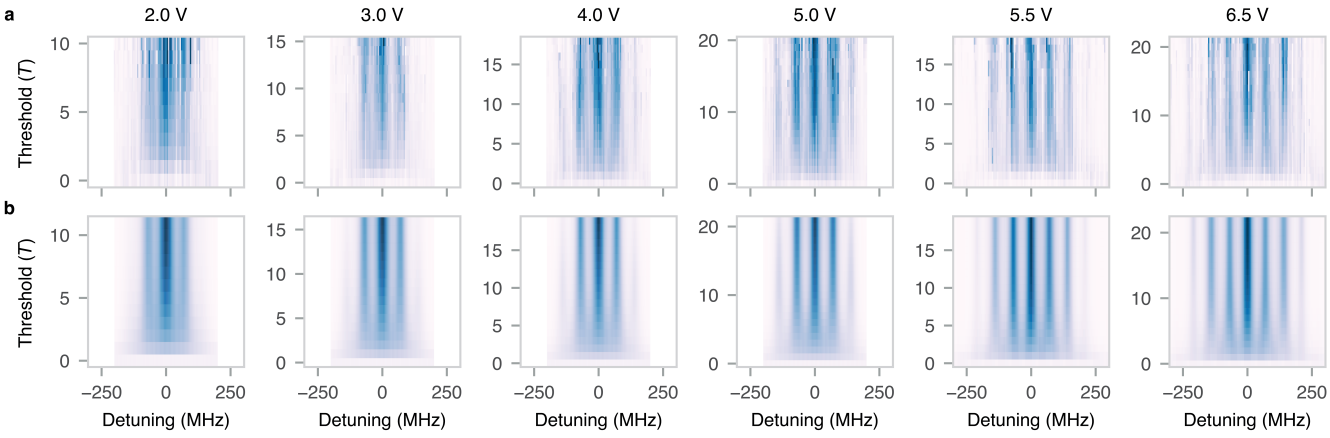

Supplementary Figure 6. **Bayesian analysis of the LZS interference signal. a)** Experimental data underlying the extracted parameters presented in Fig. 5i and j (applied voltage annotated), as a function of the two-laser detuning ($f_2 - f_1$) and the set threshold T. **b)** Fit of the data in (a) to Eq. S14, using only three free fit parameters: A, Ω and T_2, together with a general scaling and offset. The fixed fit parameters ω and T_1 are set to 70 MHz and 7 ns, respectively. The dependence on T is fixed by the model (Eq. S11).

Supplementary Note 5. Mean linewidth approximation

As noted in the main text, for the check-probe spectroscopy experiments that are executed with the MW mixing instead of the two NIR lasers, there is an approximately equal chance of initialising the system on the A_1 transition, or the A_2 transition. Hence, we expect the observed spectrum to be a (weigthed) average of both spectra, weighted by the respective initialisation probabilities. Assuming near-equal brightness of the transitions [2], we approximate this weighting to be roughly $50/50$.

To compare the measured linewidth (after accounting for residual inhomogeneous broadening, see Supplementary Note 4), with the expected lifetime limit, we approximate the weigthed mean of the two Lorentzian transitions, to be a Lorentzian with linewidth given by the weighted mean of the respective linewidths:

$$\Gamma = p\Gamma_{\mathrm{A}_1} + (1-p)\Gamma_{\mathrm{A}_2} \tag{S15}$$

with p the probability of initialising on the A_1 transition, and $\Gamma_{\mathrm{A}_1} \approx 26\,\mathrm{MHz}$ and $\Gamma_{\mathrm{A}_2} \approx 14\,\mathrm{MHz}$ the linewidths (FWHM) of the A_1 and A_2 transitions, respectively [2]. For these values, Eq. S15 approximates the true linewidth with deviation less than 5% (Supplementary Fig. 7b).

A more rigorous treatment for estimating the individual A_1 and A_2 linewidths consists of explicitly specifying both transitions (separated by $\Delta \approx 1\,\mathrm{GHz}$) with their respective amplitudes and lifetimes in the spectral response function $\lambda(f)$ (instead of using Eqs. 4 and 6). A more straightforward solution is to use an additional third laser (not available in this work) to perform the 'check' block as is done in Fig. 3a, which leaves no ambiguity for the initialisation configuration. Both the A_1 or A_2 transitions can then be measured individually by using a single NIR laser (together with the MW radiation) to probe around the two laser frequencies used in the 'check' block.

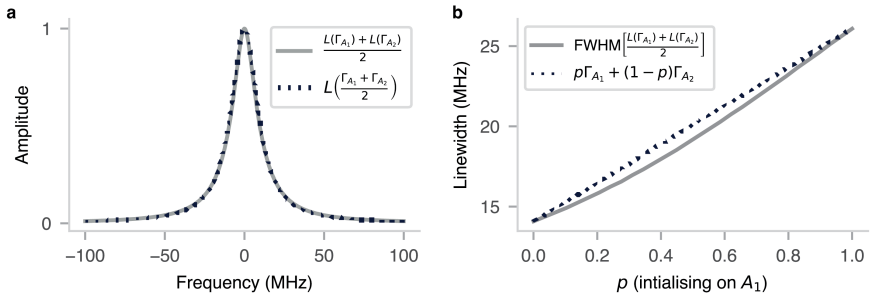

Supplementary Figure 7. **Mean linewidth approximation. a)** Comparison between the equal mean of two Lorentzians with FWHM $\Gamma_{\mathrm{A}_1} = 26\,\mathrm{MHz}$ and $\Gamma_{\mathrm{A}_2} = 14\,\mathrm{MHz}$ (grey line) and a single Lorentzian function with a FWHM of $\Gamma = \frac{\Gamma_{\mathrm{A}_1}+\Gamma_{\mathrm{A}_2}}{2} = 20\,\mathrm{MHz}$ (blue dotted line), showing qualitative agreement ($< 1\%$ amplitude deviation). Legend: $L(\Gamma)$ denotes the Lorentzian distribution with FWHM Γ. **b)** Numerically determined linewidth (FWHM) of the weighted mean (with weights p and $1-p$) of two Lorentzians with FWHM Γ_{A_1} and Γ_{A_2} as in (a) (grey line). The blue dotted approximates the actual linewidth by a (linear) weighted mean (Eq. S15), showing deviations of less than 5%.

Supplementary Note 6. Spectral diffusion dynamics during 'scanning' PLE

Complementary to the measurements in Fig. 4, we perform repetitive PLE linescans of a V2 center (as in Refs. [3–7], among others). This is a different V2 center than the one studied in the main text, in particular, it resides in a different sample diced from the same wafer, but electron-irradiated at a slight lower dose of $2 \times 10^{12}\,\mathrm{cm}^{-2}$. For fair comparison, we include the diffusion-averaged PLE measurement, and the NIR-lasers diffusion measurement (see Fig. 1f and as in Fig. 3d of main text) in Supplementary Fig. 8. These measurements indicate large diffusion-averaged linewidth and a high spectral diffusion rate $(8(2)\,\mathrm{GHz/s})$. As noted in earlier work [3, 6, 7], summing individual scans may result in underestimation of the homogeneous linewidth due to limited photon statistics [6], or to overestimation of the linewidth if the emitter frequency changes during, and in between, repetitions. From the spectral diffusion measurements we can roughly distill the diffusion timescale to be $\sim 10\,\mathrm{ms}$. Since a single PLE linescan cannot be performed (with our current hardware) faster than the diffusion timescale, we limit the time during which the NIR laser is on. We scan the frequency by ramping an external voltage to the cavity of the laser $(1.4\,\mathrm{V})$. Each PLE scan takes $500\,\mathrm{ms}$, where each voltage step $(19\,\mathrm{mV})$ the NIR-laser is turned on for $1\,\mathrm{ms}$ with $10\,\mathrm{nW}$ of power, resulting in a total NIR-laser time of $71\,\mathrm{ms}$ during a single repetition.

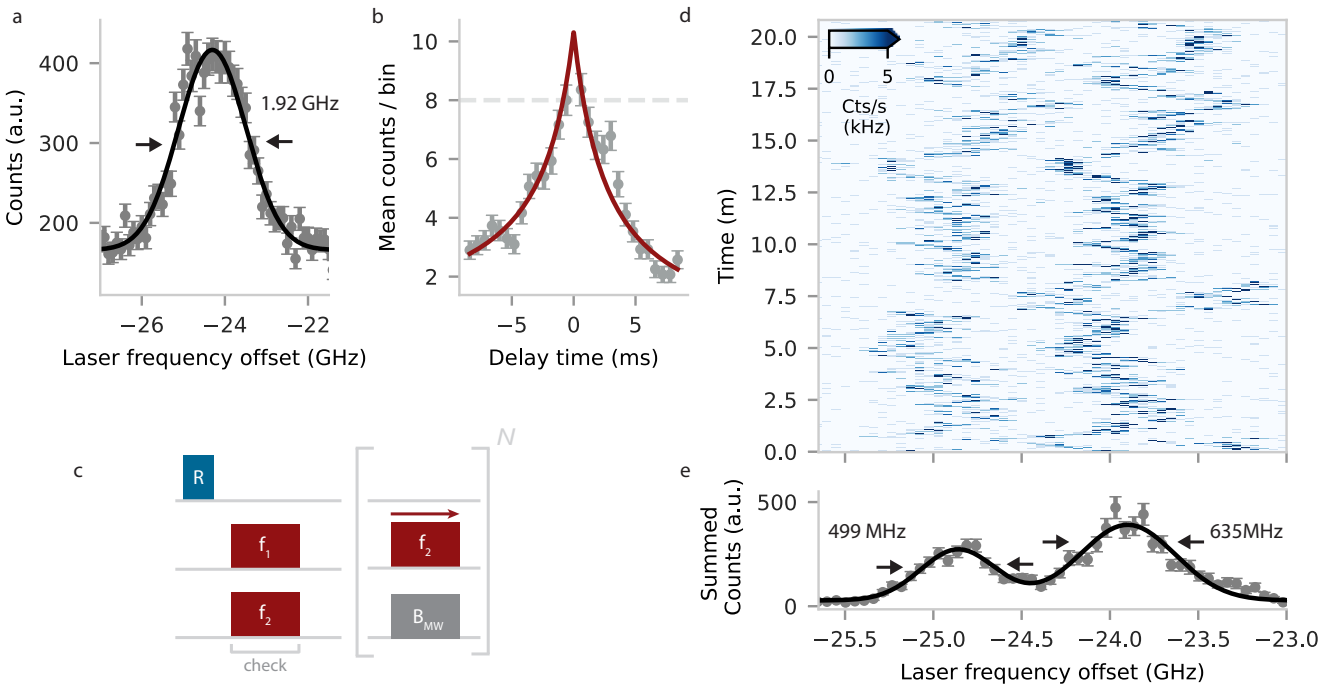

Supplementary Figure 8. **Spectral diffusion during repetitive NIR-laser PLE scans. a)** Diffusion-averaged broadening of the defect in a different nanopillar (in a different sample) compared to the main text with $\sim 1.92\,\mathrm{GHz}$ FWHM. **b)** Spectral diffusion measurement and fit under 10 nW of NIR laser excitation (916 nm) (same measurement as Fig. 3). **c)** Experimental sequence used for the repetitive-scanning experiment. A 'check' block is executed until the collected counts exceed a set threshold (here T = 30). Subsequently, the f_2 laser is scanned by ramping an external voltage to the cavity of the laser $(1.4\,\mathrm{V})$, while applying microwave resonant with the ground-state spin transition $(6\,\mathrm{V}$, different wire-sample distance compared to main text) with $N = 500$ scans. Each scan takes $500\,\mathrm{ms}$, where each voltage step $(19\,\mathrm{mV})$ the resonant laser is turned on for $1\,\mathrm{ms}$ with $10\,\mathrm{nW}$ of power, resulting in a total resonant laser time of $71\,\mathrm{ms}$ during a single repetition. Before and after the voltage scan, the laser frequency is measured $(1\,\mathrm{s})$ and a linear extrapolation between the start end and frequency is created to convert the applied voltage to an applied laser frequency. **d)** 500 PLE scans of the same defect as in b). Each repetition, the laser is scanned over $\sim 3\,\mathrm{GHz}$). **e)** Summed counts of all the repetitions, indicating the A1 and A2 transition at $-24.86\,\mathrm{GHz}$ and $-23.90\,\mathrm{GHz}$ respectively, with FWHMs of $499(14)\,\mathrm{MHz}$, and $635(11)\,\mathrm{MHz}$, respectively (Gaussian fit). The laser frequency is offset to $327.112\,\mathrm{THz}$.

Supplementary Note 7. Confocal microscopy setup

In Supplementary Fig. 9 the schematics of the optical setup is shown, which is divided into two parts, in-fiber (left) and free-space (right). The electronics are not depicted in the figure.

In Fiber: Two NIR lasers (916 nm, Toptica DL Pro and the Spectra-Physics Velocity TLB-6718-P, are frequency-locked to a wavemeter (HF-Angstrom WS/U-10U), using a 99:1 beamsplitter. Their optical power is modulated by acousto-optic-modulators (AOM, G&H SF05958). The power of the 785 nm repump laser (Cobolt 06-MLD785) is directly controlled via analog modulation. A wavelength division multiplexer (WDM, OZ Optics) combines the 785 nm repump and 916 nm NIR laser light, after which the light is coupled out to free space using a zoom fiber collimator (Thorlabs, ZC618APC).

Free Space: The collimated beam passes through a variable neutral density filter (ND, Thorlabs NDC-50C-4-B), after which a shortpass filter (Semrock, FF01-945/SP-25) is used to remove any residual noise from the NIR lasers. A $\frac{\lambda}{2} - \frac{\lambda}{4}$ waveplate combination allows for polarisation control. The excitation path and detection path are separated with a broadband 90:10 beamsplitter (Thorlabs, BS041).

A flip mirror and 50:50 pellicle beamsplitter (Thorlabs, BP150) enable imaging of the sample with a visible LED (MCWHL6-C2) and a CCD-camera (ClearView Imaging, BFS-U3-16S2M-CS).

A 0.9 NA microscope objective (Olympus, MPLFLN 100x) is used to focus excitation light onto the nanopillars, and to collect fluorescence. The objective is kept at room temperature and under vacuum, and can be moved using a configuration of 3 piezo-electric stages (PI Q545.140). The sample is cooled down to 4 K in a cryostat (Montana Instruments S100), while a heat shield kept at 30 K limits thermal radiation from the objective.

Collected fluorescence passes through a 90:10 beamsplitter, after which it can be routed either to a spectrometer (Princeton Instruments IsoPlane 81), filtered with an 830 nm long-pass filter (Semrock, BLP01-830R-25), or to an avalanche photon detector (APD, Laser components, COUNT-50N) with an expected detection efficiency of 35% at 920 nm and 18% at 1000 nm. Next to a 830 nm long pass filter, an additional long-pass filter (Semrock, FF01-937/LP-25), placed at an angle, is used to filter out reflected light originating from the NIR lasers (916 nm).

Electronics Microwave pulses are generated with an arbitrary waveform generator (Zurich Instruments, HDAWG8), and subsequently amplified (Mini-circuits LZY-22+). A bondwire is spanned across the sample to deliver the MW radiation close to the sample surface ($\sim$ 50 µm). The coarse time scheduling (1 µs resolution) of the experiments is managed by a microcontroller (ADwin Pro II).

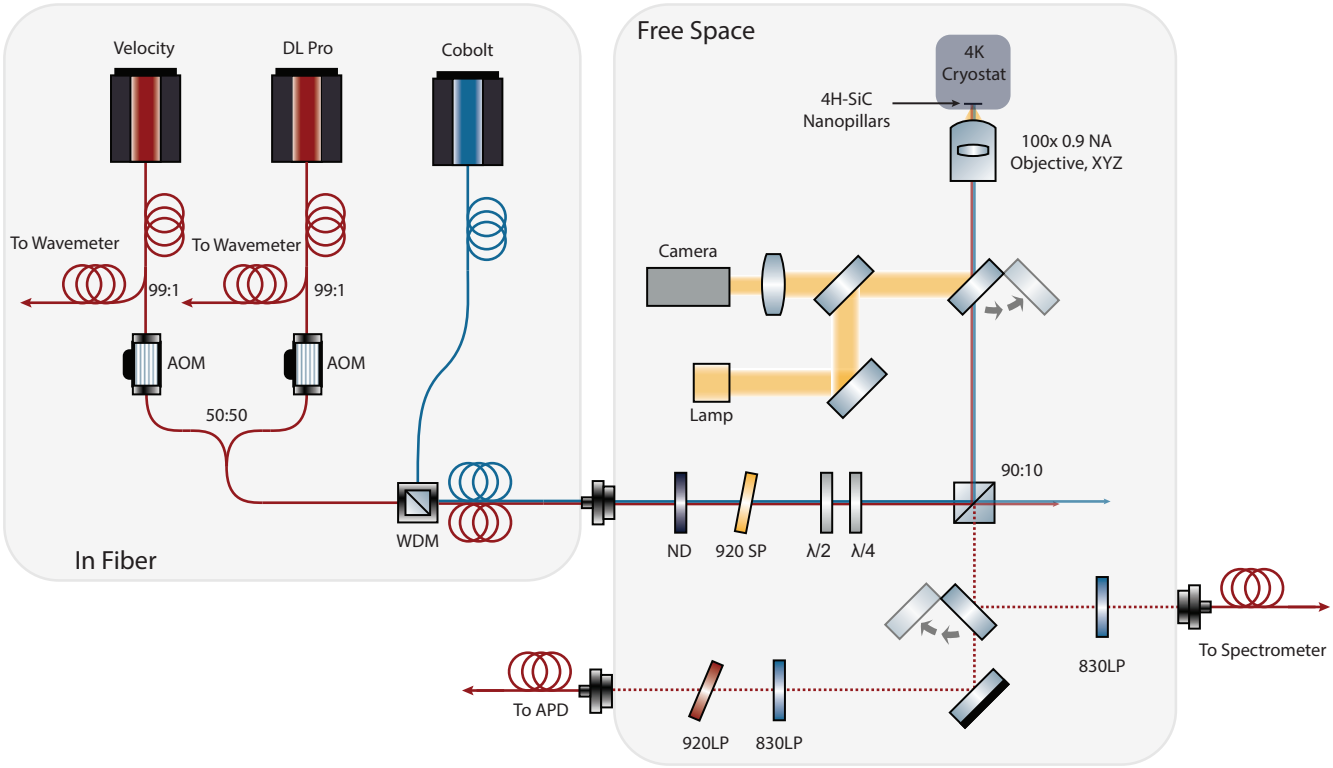

Supplementary Figure 9. **Optical setup:** Description of elements is given in the text.

Supplementary Note 8. Literature review on silicon carbide quantum emitter linewidths

In this section we provide an overview of the work done using silicon vacancies and divacancies in silicon carbide in the context of optical coherence. In table II, we report on multiple parameters that can impact the optical coherence. These parameters include the defect generation method, the annealing strategy, the measured optical absorption linewidth, material parameters of the layer that contains the investigated defect, and the use of a potential nanostructure for efficient light extraction.

Work	Defect	Defect generation	Annealing	PLE linewidth	Sample parameters in the defect layer	Nanostructure
Banks 2019[8]	V2	e: 1e12 cm^{-2}, 2 MeV	-	∼65 MHz	18µm n-doped epi layer. [N]=∼3e14 cm^{-3}	-
Nagy 2019 [9]	V1	e: 1e12 cm^{-2}, 2 MeV	30 m, 600℃	∼60 MHz	110µm [^{28}Si]>99.85%, [^{13}C]>99.98% epi layer. [N] = ∼3.5e13 cm^{-3}	SIL
Udvarhelyi 2020 [10]	V1 & V2	e: 1e13 cm^{-2}, 2 MeV	30 m, 600℃	∼100 MHz	110µm [^{28}Si]>99.85%, [^{13}C]>99.98% epi layer. [N]=∼3.5e13 cm^{-3}	SIL
Nagy 2021 [11]	V2	e: 1e13 cm^{-2}, 2 MeV	-	∼300 MHz*	[N]=∼5e13 cm^{-3}	-
Babin 2022 [4]	V2	He^{+}: 1e11 cm^{-2}, 6 keV	30 m, 600℃	∼25-40 MHz	110µm [^{28}Si]>99.85%, [^{13}C]>99.98% epi layer. [N]=∼4e13 cm^{-3}	-
Babin 2022 [4]	V2	e: 5e11 cm^{-2}, 2 MeV	30 m, 600℃	Best: ∼30 MHz	28µm [^{28}Si]>99.85%, [^{13}C]>99.98% epi layer. [N]=∼3e15 cm^{-3}	Triangular waveguides
Lukin 2020 [12]	V2	e: 1e13 cm^{-2}, 2 MeV	30 m, 300℃	∼100 MHz	100µm $^{28}Si^{13}C$ epi layer.	-
Lukin 2020 [12]	V2	e: 5e12 cm^{-2}, 23 MeV	30 m, 300℃	∼100 MHz	100µm $^{28}Si^{13}C$ epi layer.	-
Lukin 2023 [13]	V2	e: 1e13 cm^{-2}, 2 MeV	2 h, 550℃†	∼40 MHz	20µm n-doped epi layer. [N]=∼2e13 cm^{-3}	Disk resonator
Fang 2023 [14]	V1	e: 2.3e12 cm^{-2}, 10 MeV	30 m, 500℃	∼60 MHz	80µm epi layer. [N]=∼2e13 cm^{-3}	SIL
Christle 2017 [15]	VV	e: 5e12 cm^{-2}, 2.5 MeV	30 m, 750℃	∼2 GHz	730 µm sublimation epitaxially grown 3C-SiC layer. [N]∼5e15 cm^{-3}	-
Christle 2017 [15]	VV	e: 5e12 cm^{-2}, 2 MeV	30 m, 745℃	∼100 MHz	120 µm 4H-SiC epi layer. [N]<5e13 cm^{-3}	-
Miao 2019 [16]	VV	e: 3e12 cm^{-2}, 2 MeV	30 m, 850℃	∼21 MHz	20µm i-type epi layer. [N]<1e15 cm^{-3}	-
Anderson 2019 [5]	VV	-	-	∼31 MHz	-	-
Crook 2020 [17]	VV	e: 1e16 cm^{-2}, 2 MeV	30 m, 850℃	∼4 GHz	n-p-n-i-n epi layers. ($[N_n]$=1e18, $[Al_p]$=1e18, $[N_i]$<1e15) cm^{-3}	Photonic crystal cavity
Anderson 2022 [18]	VV	e: 1e13 cm^{-2}, 2 MeV	810℃	<0.5 GHz	90µm [^{28}Si]>99.85%, [^{13}C]>99.98% epi layer. [N]=∼6e13 cm^{-3}	No nanostructure

Supplementary Table II. Sample parameters on literature publications that demonstrated PLE measurements with silicon vacancy (V1, V2) defects and divacancy (VV) defects in silicon carbide. A dash (-) indicates the information is not specified in the respective publication. *: Increased linewidth attributed to global sample properties, such as an increased Fermi level due to the elevated [N], rather than defect density. †: Annealing tailored to HSQ bonding for sample preparation.

[1] G. Zumofen and J. Klafter, Spectral random walk of a single molecule, Chemical Physics Letters **219**, 303 (1994).

[2] D. Liu, F. Kaiser, V. Bushmakin, E. Hesselmeier, T. Steidl, T. Ohshima, N. T. Son, J. Ul-Hassan, Ö. O. Soykal, and J. Wrachtrup, The silicon vacancy centers in SiC: Determination of intrinsic spin dynamics for integrated quantum photonics, npj Quantum Inf **10**, 72 (2024).

[3] J. Heiler, J. Körber, E. Hesselmeier, P. Kuna, R. Stöhr, P. Fuchs, M. Ghezellou, J. Ul-Hassan, W. Knolle, C. Becher, F. Kaiser, and J. Wrachtrup, Spectral stability of V2 centres in sub-micron 4H-SiC membranes, npj Quantum Mater. **9**, 34 (2024).

[4] C. Babin, R. Stöhr, N. Morioka, T. Linkewitz, T. Steidl, R. Wörnle, D. Liu, E. Hesselmeier, V. Vorobyov, A. Denisenko, M. Hentschel, C. Gobert, P. Berwian, G. V. Astakhov, W. Knolle, S. Majety, P. Saha, M. Radulaski, N. T. Son, J. Ul-Hassan, F. Kaiser, and J. Wrachtrup, Fabrication and nanophotonic waveguide integration of silicon carbide colour centres with preserved spin-optical coherence, Nat. Mater. **21**, 67 (2022).

[5] C. P. Anderson, A. Bourassa, K. C. Miao, G. Wolfowicz, P. J. Mintun, A. L. Crook, H. Abe, J. Ul Hassan, N. T. Son, T. Ohshima, and D. D. Awschalom, Electrical and optical control of single spins integrated in scalable semiconductor devices, Science **366**, 1225 (2019).

[6] L. Orphal-Kobin, K. Unterguggenberger, T. Pregnolato, N. Kemf, M. Matalla, R.-S. Unger, I. Ostermay, G. Pieplow, and T. Schröder, Optically Coherent Nitrogen-Vacancy Defect Centers in Diamond Nanostructures, Phys. Rev. X **13**, 011042 (2023).

[7] M. K. Koch, V. Bharadwaj, and A. Kubanek, Limits for coherent optical control of quantum emitters in layered materials (2023), arXiv:2312.11090 [quant-ph].

[8] H. B. Banks, Ö. O. Soykal, R. L. Myers-Ward, D. K. Gaskill, T. Reinecke, and S. G. Carter, Resonant Optical Spin Initialization and Readout of Single Silicon Vacancies in 4H-SiC, Phys. Rev. Appl. **11**, 024013 (2019).

[9] R. Nagy, M. Niethammer, M. Widmann, Y.-C. Chen, P. Udvarhelyi, C. Bonato, J. U. Hassan, R. Karhu, I. G. Ivanov, N. T. Son, J. R. Maze, T. Ohshima, Ö. O. Soykal, Á. Gali, S.-Y. Lee, F. Kaiser, and J. Wrachtrup, High-fidelity spin and optical control of single silicon-vacancy centres in silicon carbide, Nat Commun **10**, 1954 (2019).

[10] P. Udvarhelyi, G. Thiering, N. Morioka, C. Babin, F. Kaiser, D. Lukin, T. Ohshima, J. Ul-Hassan, N. T. Son, J. Vučković, J. Wrachtrup, and A. Gali, Vibronic States and Their Effect on the Temperature and Strain Dependence of Silicon-Vacancy Qubits in 4H-SiC, Phys. Rev. Appl. **13**, 054017 (2020).

[11] R. Nagy, D. B. R. Dasari, C. Babin, D. Liu, V. Vorobyov, M. Niethammer, M. Widmann, T. Linkewitz, I. Gediz, R. Stöhr, H. B. Weber, T. Ohshima, M. Ghezellou, N. T. Son, J. Ul-Hassan, F. Kaiser, and J. Wrachtrup, Narrow inhomogeneous distribution of spin-active emitters in silicon carbide, Appl. Phys. Lett. **118**, 144003 (2021).

[12] D. M. Lukin, A. D. White, R. Trivedi, M. A. Guidry, N. Morioka, C. Babin, Ö. O. Soykal, J. Ul-Hassan, N. T. Son, T. Ohshima, P. K. Vasireddy, M. H. Nasr, S. Sun, J.-P. W. MacLean, C. Dory, E. A. Nanni, J. Wrachtrup, F. Kaiser, and J. Vučković, Spectrally reconfigurable quantum emitters enabled by optimized fast modulation, npj Quantum Inf **6**, 1 (2020).

[13] D. M. Lukin, M. A. Guidry, J. Yang, M. Ghezellou, S. Deb Mishra, H. Abe, T. Ohshima, J. Ul-Hassan, and J. Vučković, Two-Emitter Multimode Cavity Quantum Electrodynamics in Thin-Film Silicon Carbide Photonics, Phys. Rev. X **13**, 011005 (2023).

[14] R.-Z. Fang, X.-Y. Lai, T. Li, R.-Z. Su, B.-W. Lu, C.-W. Yang, R.-Z. Liu, Y.-K. Qiao, C. Li, Z.-G. He, J. Huang, H. Li, L.-X. You, Y.-H. Huo, X.-H. Bao, and J.-W. Pan, Experimental Generation of Spin-Photon Entanglement in Silicon Carbide, Phys. Rev. Lett. **132**, 160801 (2024).

[15] D. J. Christle, P. V. Klimov, C. F. de las Casas, K. Szász, V. Ivády, V. Jokubavicius, J. Ul Hassan, M. Syväjärvi, W. F. Koehl, T. Ohshima, N. T. Son, E. Janzén, Á. Gali, and D. D. Awschalom, Isolated Spin Qubits in SiC with a High-Fidelity Infrared Spin-to-Photon Interface, Phys. Rev. X **7**, 021046 (2017).

[16] K. C. Miao, A. Bourassa, C. P. Anderson, S. J. Whiteley, A. L. Crook, S. L. Bayliss, G. Wolfowicz, G. Thiering, P. Udvarhelyi, V. Ivády, H. Abe, T. Ohshima, Á. Gali, and D. D. Awschalom, Electrically driven optical interferometry with spins in silicon carbide, Sci. Adv. **5**, eaay0527 (2019).

[17] A. L. Crook, C. P. Anderson, K. C. Miao, A. Bourassa, H. Lee, S. L. Bayliss, D. O. Bracher, X. Zhang, H. Abe, T. Ohshima, E. L. Hu, and D. D. Awschalom, Purcell Enhancement of a Single Silicon Carbide Color Center with Coherent Spin Control, Nano Lett. **20**, 3427 (2020).

[18] C. P. Anderson, E. O. Glen, C. Zeledon, A. Bourassa, Y. Jin, Y. Zhu, C. Vorwerk, A. L. Crook, H. Abe, J. Ul-Hassan, T. Ohshima, N. T. Son, G. Galli, and D. D. Awschalom, Five-second coherence of a single spin with single-shot readout in silicon carbide, Sci. Adv. **8**, eabm5912 (2022).